Acta Materialia 200 (2020) 274–286

Contents lists available at ScienceDirect

Acta Materialia

journal homepage: www.elsevier.com/locate/actamat

Full length article

Bulk nanocrystalline high-strength magnesium alloys prepared via rotary swaging

Yingchun Wan[a,d], Bei Tang[d], Yonghao Gao[d], Lingling Tang[b], Gang Sha[c], Bo Zhang[c], Ningning Liang[b], Chuming Liu[d,*], Shunong Jiang[d], Zhiyong Chen[d], Xueyi Guo[a,*], Yonghao Zhao[b,*]

[a] School of Metallurgy and Environment, Central South University, Changsha 410083, China
[b] Nano and Heterogeneous Materials Center, School of Materials Science and Engineering, Nanjing University of Science and Technology, Nanjing 210094, China
[c] Herbert Gleiter Institute of Nanoscience, Nanjing University of Science and Technology, Nanjing 210094, China
[d] School of Materials Science and Engineering, Central South University, Changsha 410083, China

ARTICLE INFO

Article history:
Received 3 June 2020
Revised 19 August 2020
Accepted 6 September 2020
Available online 11 September 2020

Keywords:
Nanocrystalline magnesium alloy
High strength
Grain refinement
Deformation mechanisms
Rotary swaging

ABSTRACT

Being lightweight, energy-efficient and environmentally benign, magnesium alloys present great potential for various industrial applications. However, they possess relatively low mechanical properties and need to be strengthened. During the last decade, significant effort has been directed towards preparation of strong nanocrystalline (NC) Mg alloys, although because of the limited plasticity inherent to HCP metals, the grain size of Mg was rarely refined below 1000 nm and the yield strength seldom exceeded 500 MPa. Here, by means of a conventional industrial method of rotary swaging, we prepared bulk NC Mg–Gd–Y–Zr alloys with an average grain size of 80 nm and a dimension of ∅3 mm × 1000 mm. The further-aged NC Mg alloy exhibits the yield strength of 650 MPa and the ultimate tensile strength of 710 MPa, the highest such values published for bulk Mg alloys. Fracture surface observation suggested a ductile inter-granular fracture in the NC Mg alloys. The high strength are attributed to nano-grain, intra-granular Gd rich clustering, inter-granular solutes segregation, β' precipitation, dislocation and solution strengthening contributions, among which the nano-grain strengthening is dominant. The nano-grain formation results from the large number of mechanical twins, deformation bands and stacking faults induced by the high strain rate of swaging. Our work advances the industrial-scale production of bulk NC Mg alloys by exploring a simple and low-cost fabrication technique.

© 2020 Acta Materialia Inc. Published by Elsevier Ltd. All rights reserved.

1. Introduction

Magnesium alloys possess great potential to improve energy efficiency and system performance in automotive, electronics and aerospace industries due to their low density (1.7 $g \cdot cm^{-3}$), excellent damping capacity, machinability, abundance and recyclability [1,2]. Nevertheless, there still exist critical issues, including relatively low strength and fracture toughness [3–16], limited deformation capability at room temperature [17] due to the hexagonal close-packed (HCP) structure and high susceptibility to corrosion, that hinder the application of Mg alloys as structural materials. Significant effort has therefore been directed during the last decade towards the solution of these problems, with some recent examples of success to look to [3,4,18–20].

Strategies for strengthening Mg alloys include either grain refinement via severe plastic deformation (SPD) [5–16] or alloying with rare earth (RE) elements followed by solid solution treatment and precipitation hardening [21,22]. The SPD processing has to be performed at elevated temperatures (usually in a range of 423 to 623 K) and the minimum grain size achieved for Mg alloys is approximately several micrometers (rarely below one micrometer), due to the limited plasticity of HCP structure. Therefore, the strengthening effect of grain refinement on bulk Mg alloys is rather modest. The highest yield strength of SPD-processed bulk Mg alloys is reported to be 610 MPa [5] and the highest compressive strengths of nanoparticle-dispersed Mg composite micro-pillars are 710 MPa (yield) [3] and 3.5 GPa (ultimate) [4]. Meanwhile, the strengthening effects from adding RE elements are limited by their solid solubility. Consequently, for coarse-grained (CG) Mg–Gd–Y–Zr

* Corresponding authors.
E-mail addresses: cmliu@csu.edu.cn (C. Liu), xyguo@csu.edu.cn (X. Guo), yhzhao@njust.edu.cn (Y. Zhao).

https://doi.org/10.1016/j.actamat.2020.09.024
1359-6454/© 2020 Acta Materialia Inc. Published by Elsevier Ltd. All rights reserved.

alloy, the yield strength seldom exceeds 480 MPa, and is usually of the order of ~400 MPa [21,22]. Moreover, the SPD processing of Mg alloys is usually expensive, complex and inefficient; the highest dimension of specimens produced is normally of the centimeter or even millimeter scale, being difficult to scale further up. Current nanocrystalline (NC) Mg alloys with <100 nm grain sizes were normally obtained through high pressure torsion (HPT) or surface mechanical attrition treatment (SMAT) methods, which could only produce slices or sheets with < 1 mm thickness [4,12,23].

In the present study, we employed rotary swaging, a conventional industrial method, to prepare bulk high-strength NC Mg–8Gd–3Y–0.4Zr (wt%) alloy rods with an average grain size of 80 nm. By further aging the NC Mg alloy, we obtained the yield strength of 650 MPa and the ultimate tensile strength of 710 MPa.

2. Experiments

2.1. Sample preparation and aging process

A Mg–8Gd–3Y–0.4Zr (wt%) alloy ingot with a dimension of ∅130 mm × 1000 mm was prepared by melting high-purity magnesium, 30% Mg–Gd, 30% Mg–Y and 30% Mg–Zr (wt%) alloys in a mild steel crucible and casting in an upright semi-continuous cast machine. The ingot was first homogenized at 813 K for 15 h, and then extruded at 723 K into bar billets of 18 mm in diameter for subsequent swaging. One up to four passes of rotary swaging was finally carried out at room temperature to get diameters of 17.5, 16.5, 15.5 and 14.5 mm (corresponding area reductions of 6, 16, 26 and 35%), respectively. The subsequent aging processes were performed at 338 K for 72 h in a furnace with Ar gas as protecting atmosphere.

2.2. Mechanical tests

Vickers micro-hardness test was performed using a HMV-G 21DT (Shimazdu, Japan) tester with a load of 4.9 N and a dwell time of 15 s. An Instron 3369 machine was employed to perform tensile tests at room temperature in direction parallel to the bar axis, at a strain rate of 1×10^{-3} s^{-1}. The dog bone-shaped cylinder specimens for tensile testing were turning machined from the four-pass swaged sample. We machined two types of tensile specimens. One has gauge dimensions of ∅8 mm × 40 mm which includes NC and ultrafine grained (UFG) Mg alloys (regions I+II) by turning machining away the outer part (with the thickness of 3.7 mm in diameter) of the swaged sample. Another has gauge dimensions of ∅3 mm × 15 mm which only includes NC Mg alloys (region I) in the center part of the swaged sample by machining off the outer part with the thickness of 8.7 mm in diameter. The detailed defination of region I, II and III can be referred to Fig. 2c in result section. The strain was measured by using a standard non-contacting video extensometer. Three tensile specimens were tested to obtain reliable results.

2.3. Microstructural and compositional characterizations

Transmission electron microscopy (TEM) and high resolution TEM (HRTEM) observations were carried out using a Tecnai G^2 F20 microscope, with samples being thinned by twin-jet polishing to an electron-transparent thickness in an aqueous electrolyte containing 1 vol% nitric acid, 2 vol% perchloric acid and 97 vol% ethanol. Scanning electron microscopy (SEM) observations of freshly fractured surfaces were performed using a Sirion 200 microscope immediately after the tensile tests to avoid oxidation.

The atom probe tomography (APT) specimens were prepared by a conventional electro-polishing method. The APT measurements were performed with a local electrode atom probe (LEAP 4000X Si) under UV laser pulsing at laser energy of 40 pJ, a pulse repetition rate of 200 kHz and a target evaporation rate of 0.5% per pulse at 25 K. The reconstruction and quantitative analysis of APT data were performed using a CAMECA visualization and analysis software (IVAS 3.6.8).

3. Results and discussions

3.1. Microstructures of extruded and swaged Mg alloys

An initially used CG Mg–Gd–Y–Zr rod with a diameter of 18 mm was first prepared via semi-continuous casting with subsequent homogenization and thermal extrusion. Fig. 1 shows optical micrographs of the extruded rod viewed from top (Fig. 1A) and side (Fig. 1B) planes. One can see the extruded Mg alloys have homogeneous microstructures in top plane (Fig. 1A) with dynamic recrystallized (DRX) equi-axed grains of α-Mg solid solution and an average grain size of 8 μm. In the side plane as shown in Fig. 1B, larger recrystallized equi-axed α-Mg grains with an average size of 12 μm can be discerned, and at the same time a small number of deformation traces with small recrystallized grains can be seen, as pointed out by white arrows. The X-Ray diffraction pattern in Fig. 1C revealed the main α-Mg phase with HCP structure and small amount of RE-rich phase.

The extruded rods were then rotary swaged at room temperature for four passes to a final rod with 14.5 mm in diameter (a cross-area reduction of 35%) and a length of 1 m. Fig. 2A shows the schematic representation of swaging process and Fig. 2B is the picture of the swaged Mg alloy rod. During rotary swaging, the rod was deformed under a high strain rate of approximately $10–10^2$ s^{-1} and a high hydrostatic stress from the die impacts. As shown in Fig. 2C, the micro-hardness in top plane of the CG extruded Mg alloy was ~0.9 GPa, whereas the four-pass swaging resulted in a gradient distribution of micro-hardness along the radial direction, with a constant value of ~1.3 GPa in the central region (defined as region I with radius r smaller than 1.5 mm), which then decreases gradually to approximately 1.1 GPa as r increases to 4 mm (defined as region II) and remains unchanged at 1.1 GPa with r larger than 4 mm (defined as region III). Transmission electron microscopy (TEM) revealed that region I (denoted as “NC Mg alloy” below) was composed of equi-axed nano-grains with an average size of approximately 80 nm (Fig. 2D and Fig. 3C). Selected area electron diffraction (SAED) pattern showed a ring-like pattern (inset in Fig. 2D), indicating that most of the grains were randomly oriented and separated by high-angle grain boundaries (GBs). The non-uniform deformation contrast in the most of nano-grains suggests the majority of nano-grains were formed via deformation but recrystallization. Fig. 2E shows high resolution TEM (HRTEM) image of three grains with high-angle GBs. The basal plane (0002) was marked in grains 1 and 2, and prismatic plane (10–11) was marked in grain 3.

Except the microhardness and microstructural characterizations in top plane of the swaged Mg alloys, we also performed the same measurements in side plane, as shown in Fig. 3. From Fig. 3A, there is not evident difference in microhardness between the top and side planes of the extruded Mg alloys. However, for the swaged Mg alloys, the microhardness in side plane of region I is smaller than that in top plane. Bright-field TEM in Fig. 3B revealed lamella grains with an average width of 90 nm (Fig. 3D) in side plane of the swaged Mg alloys which explains the reason for the smaller microhardness. The SAED pattern revealed both high angle and low angle GBs. The non-uniform contrast in lamella grains further confirmed the conclusion that the nano-grains were formed via deformation but recrystallization. Therefore, the swaged Mg alloys are anisotropic in terms of properties and microstructures.

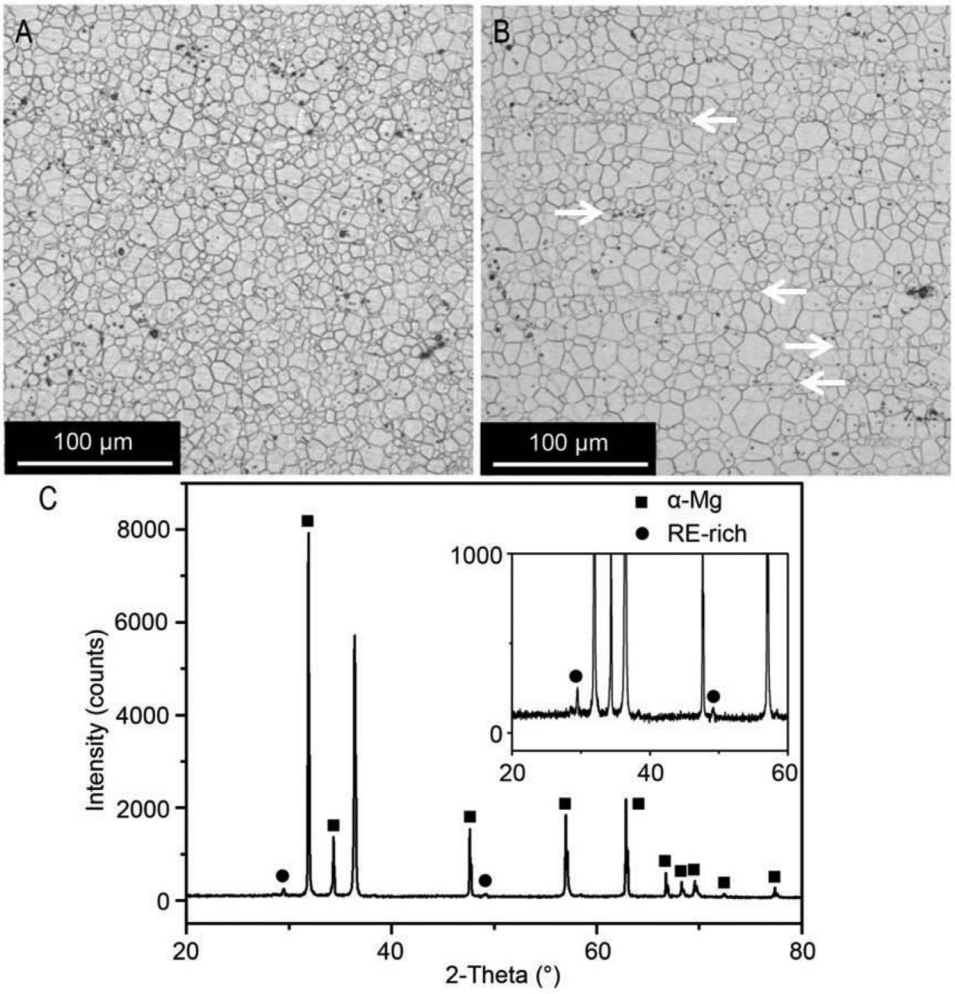

Fig. 1. Microstructure and phase contents of the as-extruded CG Mg alloy. (A and B) Optical micrographs of the extruded rod viewed from top (A) and side (B) planes, showing homogeneous dynamic recrystallized (DRX) α-Mg solid solution. (C) X-Ray diffraction pattern revealing α-Mg and RE-rich phase.

Fig. 4 displays TEM images of microstructures in region III (most out part) of the swaged Mg alloy. Both deformation twins and dislocation cells can be discerned in Fig. 4A. Fig. 4B is the magnified TEM image of area "B" in (A) clearly showing dislocation cells. Fig. 4(C, D) are SAED pattern and index of the SAED pattern approving the existence of deformation tension twins. In the transition region II, we observed a mixed area which was composed of regions of deformation bands with low-angle GBs (as marked in Fig. 5A), nano-grains and deformation twins (as shown in Fig. 5C). The blue and yellow dot-lines in Fig. 5A refer to the primary and secondary band boundaries, respectively. Fig. 5B is typical HRTEM image in area of Fig. 5A which illustrates a 5° small-angle GB formed by dislocation arrangement, as marked by "⊥". The inset in Fig. 5B is Fourier transformation of the HRTEM image.

3.2. Microstructures of aged NC Mg alloys

In order to optimize mechanical properties of the age-hardenable swaged Mg–Gd–Y–Zr alloy, we performed isothermal aging to the swaged samples at different temperatures (448-498 K). The microhardness aging curves versus aging time at different aging temperatures of the NC Mg alloy are shown in Fig. 6A. The aging curves demonstrate the lower the aging temperature, the higher the hardness peak and the longer aging time for the peak hardness. We achieved the maximum hardness of 1.55 GPa at the aging temperature of 448 K and time of 72 h (Fig. 6A). The gradient microhardness in radial direction of the aged swaged Mg alloy was drawn in Fig. 2C. One can see low-temperature aging moves the whole curve upwards about 0.3 GPa. Subsequent TEM analysis revealed that such a low-temperature aging did not change the grain size in region I (Fig. 6B) but precipitated β' phase in the nano-grain interior, as further revealed in the diffraction pattern generated by Fourier transformation of the HRTEM image in Fig. 6C [24,25].

3.3. Mechanical properties of swaged and aged NC Mg alloys

To evaluate the mechanical properties of the swaged and aged Mg alloys, we performed uniaxial tensile tests. The engineering stress-strain curves are shown in Fig. 7A. The extruded CG sample exhibited a yield strength of approximately 200 MPa and a ductility of 14%, as listed in Table 1. After the swaging process, the Mg alloy containing both regions I and II had a yield strength of 430 MPa and a ductility of 8%, and that in region I only, containing nano-grains, showed a remarkably high yield strength of 560 MPa, with the ultimate strength and uniform elongation as well as ductility of 630 MPa, 3% and 5%, respectively. The aging process further increased the yield and ultimate strength as well as uniform elongation in the region I to 650 and 710 MPa as well as 4%, while slightly decreasing the ductility to 4.5%. Fig. 7B compares our results with the yield strength versus ductility data for other bulk processed Mg alloys in the literature [5–16], indicating

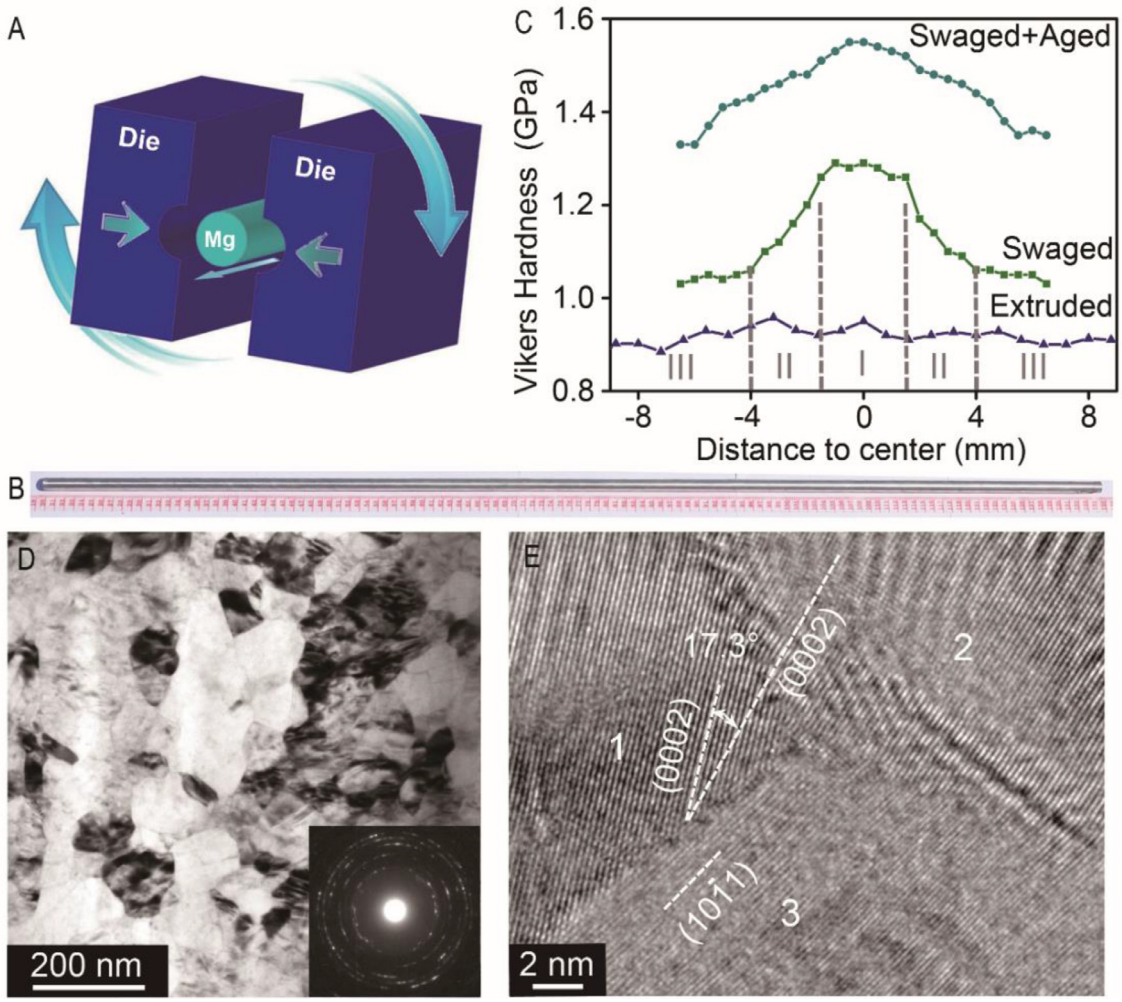

Fig. 2. Processing, hardness and microstructures in top plane of the swaged Mg alloys. (A) Schematic illustration of the rotary swaging technique. (B) Picture of the swaged sample. (C) Vickers micro-hardness measured from center to edge in top plane along the radial direction of the swaged and extruded Mg alloy rods, where three regions (marked as I, II and III) are distinguished. (D) Bright-field TEM image of region I. The inset is the corresponding SAED pattern. (E) HRTEM image showing high-angle GBs between grains 1, 2 and 3. The basal plane (0002) was marked in grains 1 and 2, and prismatic plane (10-11) was marked in grain 3.

Table 1
Lists of yield strength (YS), ultimate tensile strength (UTS), uniform elongation ε_{ue} and elongation to failure ε_{ef} of the CG, swaged region I, swaged regions I+II, swaged and aged region I Mg alloys.

Samples	YS, MPa	UTS, MPa	ε_{ue}, %	ε_{ef}, %
CG Extruded	200	320	14	14
Swaged regions I+II	430	470	6	8
Swaged region I	560	630	3	5
Swaged+aged region I	650	710	4	4.5

that our values surpass those reported in previous studies. Since aging did not change the grain size in region I, the increase in Mg alloy strength could be mainly attributed to the formation of intragranular solute clusters (as revealed by the results of 3D atomic probe tomography below) and β' precipitates which also slightly increase strain hardening capability and uniform elongation.

To reveal deformation mechanisms, fractured sample surfaces were examined by SEM. The CG Mg developed deep uniform dimples with sizes of ~10 μm (Fig. 8A), whereas for the swaged NC sample containing region I, the dimples became shallow with sizes smaller than 5 μm (Fig. 8B). A closer examination revealed a large number of grains with sizes comparable to the initial nano-grains (Fig. 8C), suggesting occurrence of a ductile inter-granular fracture. Similar fracture surface morphologies were also observed in the aged NC sample (Fig. 8D and E). Relevant modeling and experimental investigations in the literature reveal that GB-mediated deformation, such as GB sliding and migration [26,27], as well as grain rotation [28] play an important role in NC materials in addition to conventional slip of lattice dislocations [29]. For the sample consisting of regions I and II, evidence of mixed fracture (large elongated dimples from region II due to shear fracture and small dimples from region I) was observed, as shown in Fig. 8F.

3.4. 3D atomic probe tomography (APT) composition analyses

3D APT was employed to determine the composition distributions of the solutes Gd, Y and Zr in Mg matrix. 3-D atomic maps of the swaged and aged samples (Fig. 9A) showed both tip specimens containing clear GBs, as marked by white arrows. 1D concentration profiles across GBs revealed segregations of Gd, Y and Zr at the GBs (Fig. 9B), while the quantitative composition analysis indicated the excess of Gd, Y and Zr at GBs in the swaged sample at 1.32, 0.34 and 0.21 atom/nm^2, respectively. The aging process lowered these values to 0.84, 0.21 and 0.13 atom/nm^2 correspondingly (Table 2). Here, the solute excess value is a parameter characterizing GB segregation and calculated based on comparison with the solute concentration in the grain interior. In the literature, GB

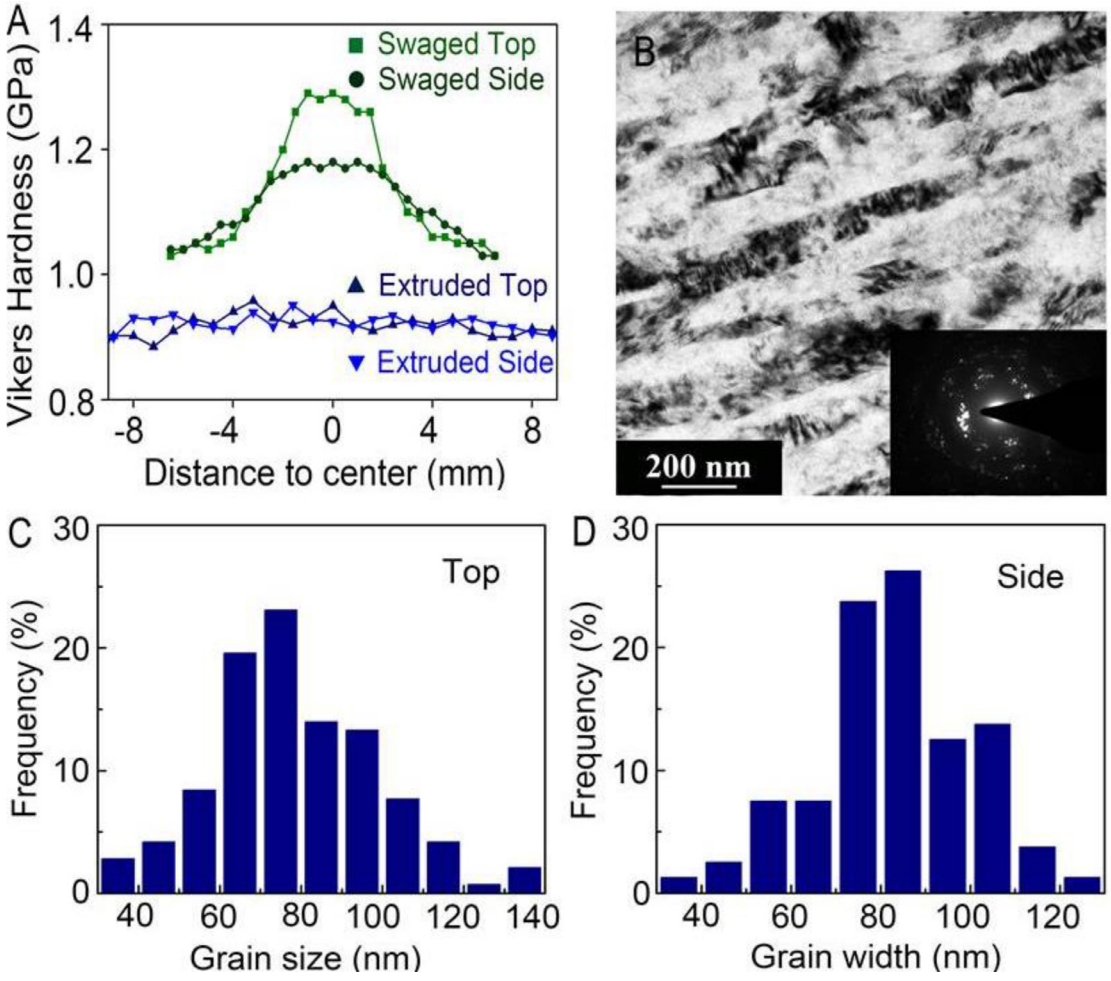

Fig. 3. Microhardness and microstructures in side plane of the swaged Mg alloys. (A) Microhardness of swaged and extruded Mg alloys in both top and side planes for comparison. (B) Bright-field TEM image of region I. The inset is the corresponding SAED pattern. (C) Grain size histogram in top plane. (D) Grain width histogram in side plane.

Table 2
Solute excess values (atoms/nm^2) at GBs of the swaged and aged Mg alloys. The error is ±0.01 atoms/nm^2.

Samples	Gd	Y	Zr
As-swaged	1.32	0.34	0.21
As-aged	0.84	0.21	0.13

Table 3
Chemical compositions (at%) of the Gd-rich clusters in the swaged and aged Mg alloys.

Samples	Mg	Gd	Y	Zr
As-swaged	86.46±4.39	8.96±3.65	1.63±1.31	1.01±0.81
As-aged	87.02±1.07	7.24±0.82	1.98±0.44	0.95±0.31

segregation is also reported in NC 7075 Al [30], Mg-Gd [31] and Ni-Mo alloys [32]. Solutes or impurities in NC materials are segregated at GBs in higher fractions/proportions than in CG materials, due to the increased GB volume fraction, short diffusion distance from the grain interior to the boundary and high density of lattice defects.

Except for solute segregation at GBs, APT also revealed Gd-rich clusters in the grain interior. Fig. 9C shows proxigrams across the matrix/cluster interfaces of the swaged and aged NC samples, and the insets are 3D atomic distributions of Gd with isosurfaces (in green) at 4 at%. The Gd concentration in the clusters (defined by their interfaces using iso-surfaces at 4 at% Gd, corresponding to the zero position of the horizontal axis in the proxigram) was approximately 9 at% for the swaged samples, and the aging process did not noticeably change the solute compositions of the Gd-rich clusters (Table 3). The number density of the Gd-rich clusters against the cluster size is shown in Fig. 9D. The aging process increased the cluster density and size, resulting in an increase of the cluster volume fraction from 14% to 34%. The above APT results indicate that deformation led to solute excess segregation at GBs, whereas aging accelerated intra-granular cluster formation, resulting in a further increase in strength.

3.5. Grain refinement mechanisms

Bulk NC Mg alloys are difficult to prepare because it is hard to avoid cracking during SPD processing; only few NC Mg alloys have so far been obtained by ball milling or surface attrition [12,33]. We further performed TEM observations (Fig. 10) to reveal formation

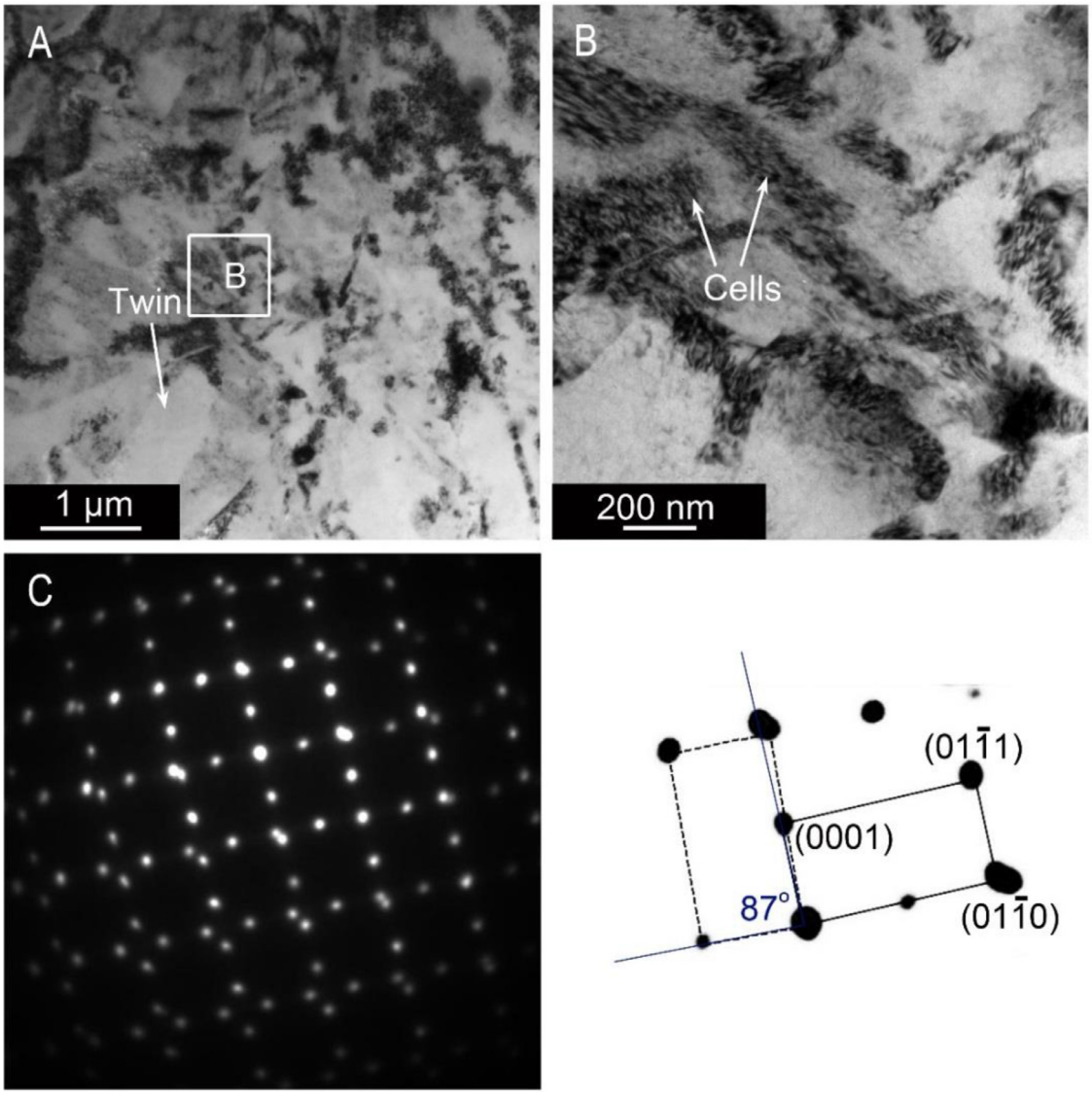

Fig. 4. Microstructures of region III in the swaged Mg alloy. (A) TEM image showing both deformation twins and dislocation cells. (B) Magnified TEM image of area "B" in (A) showing dislocation cells. (C) Selected area electron diffraction (SAED) pattern showing the existence of deformation twins. (D) Index of the SAED in (C).

mechanisms of the nano-grain structure. The NC grains were generated in two stages: (i) CG subdivision into UFGs by twinning or dislocation slipping, (ii) further refinement of UFGs down to nano-grains by stacking faults and slipping. In stage one, mechanical twining (mostly tension twining with a mis-orientation of 86.7°) firstly refined the initial CG structure into UFG plates (Fig. 10A). Dislocation slipping then divided the twin plates into finer sub-grain bands (Fig. 10B). For the non-twinned regions, the CG grains were divided by dislocation slip into primary and secondary deformation bands separated by low-angle boundaries (Fig. 10C and D). In stage two, extensive stacking faults (SFs) on (0001) basal plane and/or dislocation arrays cut the UFG bands into nano-grains (Figs. 10E and F). Further dislocation accumulation on the SFs then curved the SFs and transformed them into normal high-angle GBs [34].

We stress that the extensive generation of twin plates and deformation bands is essential to obtain a uniform deformation structure in stage (i). This is different from other works where grain refinement occurs only near GBs or twin boundary regions in Mg alloys because of the preferential dislocation generation at these boundaries and the deficiency of dislocations in long range slipping [35,36]. Moreover, our TEM observations revealed numerous non-basal slip dislocations <**c**+**a**> or <**c**> in the one-pass swaged sample (Fig. 11). An activation of non-basal slip in Mg alloys is feasible when the basal plane is titled in a way that the Schmid factor ratio of prismatic to basal slip becomes larger than 1.5–2.0 [20,37,38], the periodic variations of loading direction with high time frequency (approximately 50 Hz) might generate favorable directions for basal and non-basal co-slips and benefit the formation of deformation bands. Moreover, density-functional theory calculations and experiments also revealed that the Gd and/or Y solutes could lower the SF energy and increase the probability of non-basal dislocation slip [19,39]. Meanwhile, the high strain rate could increase the saturated dislocation density and promote the formation of twins and SFs [40]. The gradient structure is a result of the friction between the modes and the sample which created an easily-deformed zone in the central region.

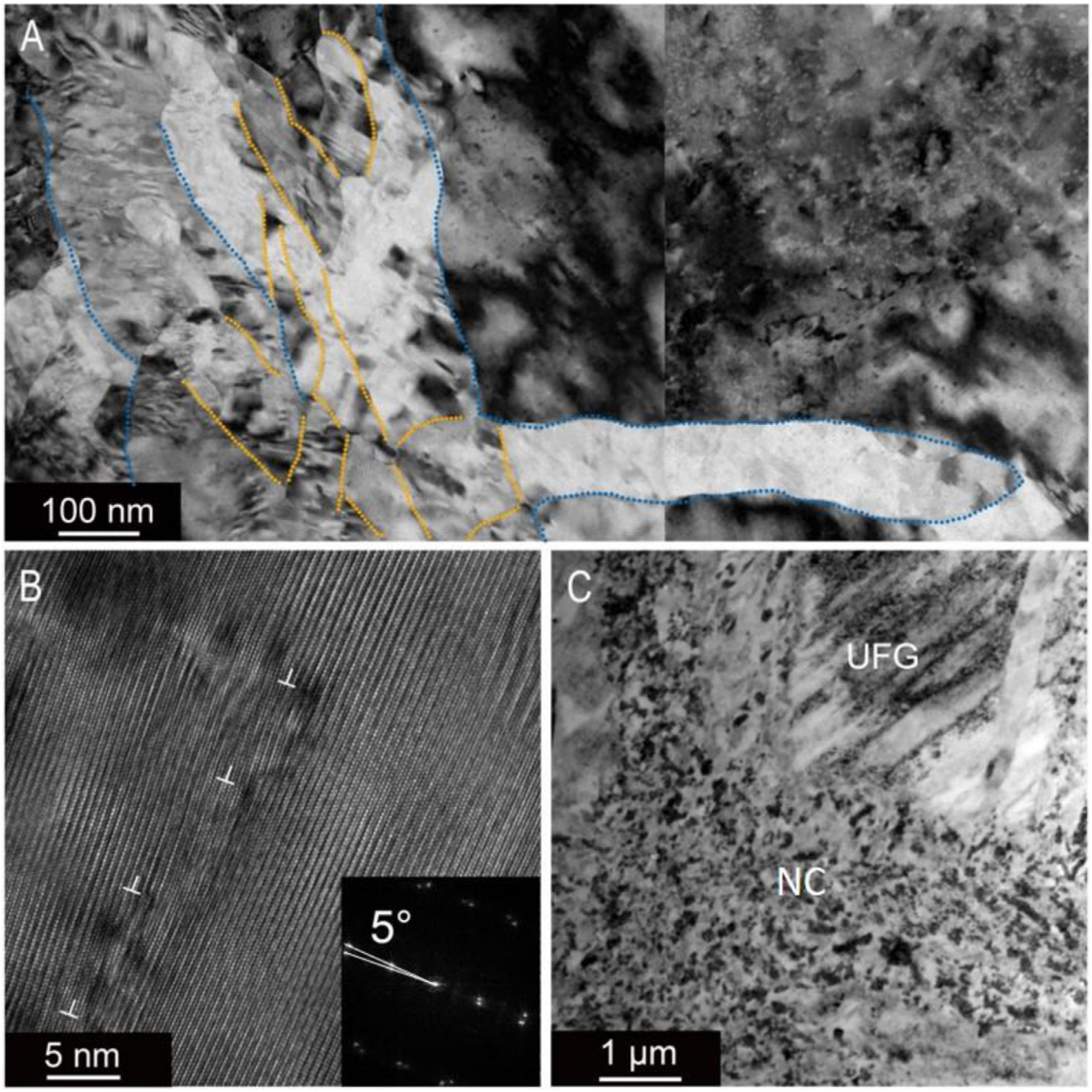

Fig. 5. TEM and HRTEM images of the swaged Mg alloy in region II. (A) Deformation band structure with low-angle GB. The blue and yellow dot-lines refer to the primary and secondary band boundaries, respectively. (B) Typical HRTEM image of the area in (A). Dislocations were marked by "⊥", and the inset is the Fourier transformation of the HRTEM image. The mis-orientation angle between two grains was about 5°. (C) TEM image of region II consisting of both NC and UFG grains. (For interpretation of the references to color in this figure legend, the reader is referred to the web version of this article.)

4. Discussions

4.1. Strength and ductility of Mg alloys

It has been reported that fine grained (1–10 μm) Mg alloys usually have better ductility than the CG (>100 μm) Mg alloys. For example, recently Huang's group reported both yield strength and ductility increase with decreasing grain size from 114 μm to 3.3 μm [37]. Our former study also found that equal channel angular pressing (ECAP) doubles both yield strength and ductility of AZ80 Mg alloys by partially refining grain size from about 50 μm down to UFG region [36]. Huang et al. further revealed that <**a**> dislocations and tension twins dominate in the samples with grain sizes larger than 10 μm, while <**a**> and <**c+a**> dislocations dominate in the samples with grain sizes smaller than 5 μm [37]. In parallel, a consistent trend for both the strength and ductility to increase with decreasing grain size is observed [37]. However, our current results in Fig. 7A and literature review in Fig. 7B indicate that with further refining grain size down to NC region (< 100 nm), Mg alloys still follow strength-ductility trade-off paradox, i.e. yield strength increases with the expense of ductility as grain size decreases down to NC and UFG regions. The decreased ductility of NC and UFG Mg alloys can be explained by fracture theory in tension [41].

Based on Hart's theory [41], during tension necking instability occurs when:

$$\Theta \leq \sigma(1-m), \tag{1}$$

where Θ is strain hardening rate, equal to $\partial\sigma/\partial\varepsilon$, m is strain rate sensitivity, equal to $\partial\ln\sigma/\partial\ln\dot{\varepsilon}$, and σ, ε and $\dot{\varepsilon}$ are true stress, true strain and strain rate. Both high Θ and m are important for high tensile ductility because they can help delay the necking and prolong the elongation. Strain hardening, i.e. dynamic strengthening during tension, is mainly resulted from interactions between dislocation and other lattice defects as well as itself, and m reflects thermally activated mechanism of slip and relates with flow stress activation volume V^*. m value of metals is usually much smaller than Θ when they deform quasi-statically at room temperature

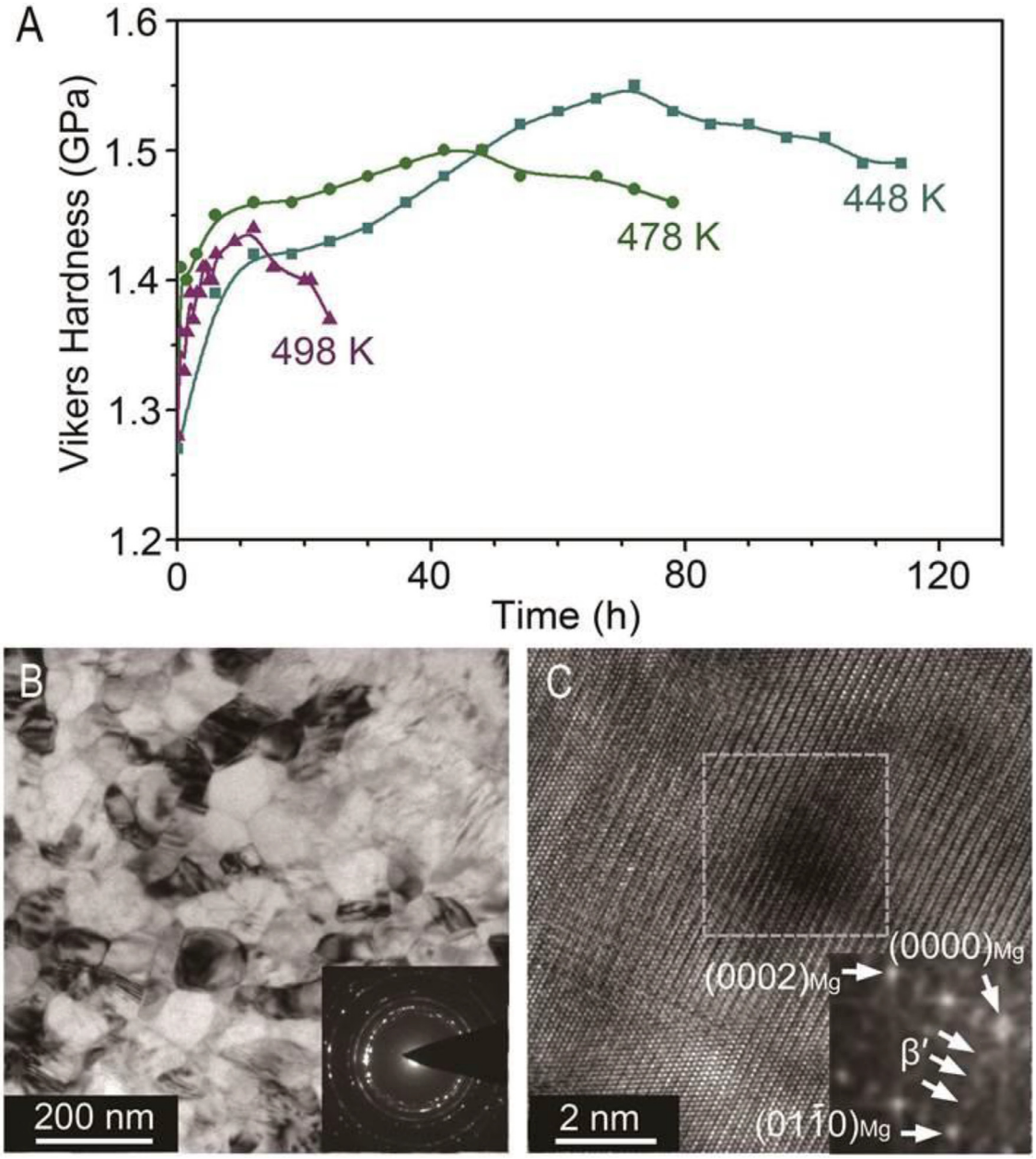

Fig. 6. Microhardness and microstructures in top plane of the aged Mg alloys. (A) Vickers hardness curves of the NC Mg alloys aged at 448, 478 and 498 K for different times. (B) TEM image of the aged NC sample at 448 K for 72 h. (C) HRTEM image of the aged NC sample. The inset is a Fourier transformation image showing extra reflection points at 1/4, 1/2, 3/4 of $(01\ 0)_{Mg}$ from β' phase.

[42]. Therefore, strain hardening capability is import and determines the overall tensile ductility. Refining the CG down to NC and UFG regions takes away the space for dislocation accumulation and multiplication, and the high density of boundaries as dislocation sinks makes the strain hardening null. Therefore, the decreased strain hardening capability and dislocation accumulation are the fundamental reasons for the low ductility of NC and UFG Mg alloys.

From Fig. 7A, it is true that for the swaged NC Mg alloy, necking appears quickly after yielding because of the low Θ. As a result, the uniform elongation is only 3%. After low-temperature aging, necking instability was postponed slightly due to dislocation recovery and β' precipitation as well as Gd-rich clustering which regained Θ more or less. The uniform elongation was also enhanced to 4.5%.

4.2. Contributions of different strengthening mechanisms

The high strength of the aged NC Mg alloy results from the following microstructural features: (i) nano-grains, (ii) high dislocation density, (iii) solid solutions of Gd and Y in the lattice, (iv) solutes (Gd, Y and Zr) segregated at GBs, (v) intra-granular solute clusters and β' precipitates.

4.2.1. Solid solution strengthening contribution

The solid solution strengthening contribution σ_s can be calculated based on the equation:

$$\sigma_s = \sigma_y + \frac{3.1\varepsilon G C^{1/2}}{700} \quad (2)$$

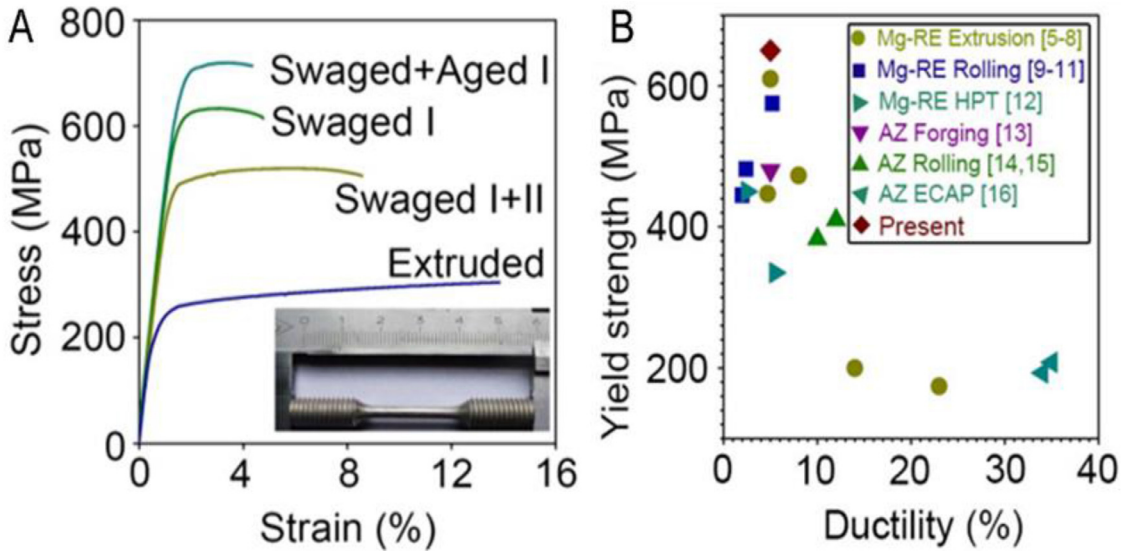

Fig. 7. Tensile properties of the swaged and aged Mg alloys. (A) Tensile stress-strain curves. (B) Comparison of yield strength versus ductility for processed Mg alloys [5-16].

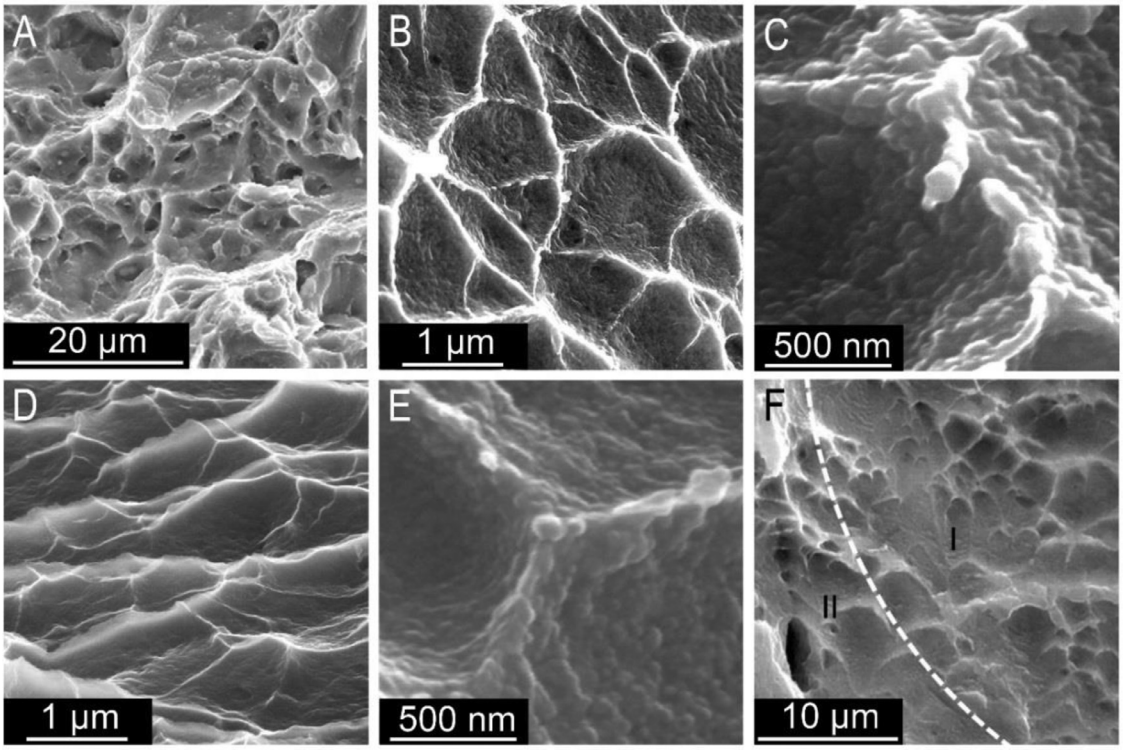

Fig. 8. SEM images of fracture surfaces. (A) CG Mg alloy. (B, C) Swaged NC Mg alloy. (D, E) Aged NC Mg alloy. (F) Swaged Mg alloys with region I and II.

where G is the shear modulus of the matrix, equal to 1.66×10^4 MPa for Mg [43], ε is an experimental constant, equal to 0.74 for Mg–Gd series alloy [24], σ_y is the yield strength of pure Mg, equal to 21 MPa [44], C is the solute concentration in atomic percentage in Mg matrix. Here C was derived from the APT results in Fig. 9C, equal to 1.88% for the aged NC Mg alloy. Thus, the solute strengthening contribution was calculated as 95 MPa.

4.2.2. Grain refinement strengthening contribution

GB strengthening contribution σ_d was calculated based on the Hall-Petch equation:

$$\sigma_d = Kd^{-1/2} \quad (3)$$

The value of K is associated with grain size d, varying in a large scale between the NC and CG alloys. K used here was derived from Ref. 3, where an increment of 300 MPa, compared with the single crystal counterpart, was obtained in the NC Mg_2Zn alloy with grain size of 105 nm. Thus, $K = \sigma_d \times d^{1/2} = 300 \times (105)^{1/2} = 3074$ MPa·nm$^{1/2}$ for NC Mg alloys, and the GB strengthening contribution was estimated as 344 MPa.

4.2.3. Dislocation strengthening contribution

Here we estimated dislocation density from XRD peak broadening [45], and calculated dislocation strengthening contribution σ_ρ from the Taylor formula [46]:

$$\sigma_\rho = M\alpha Gb\rho^{1/2} \quad (4)$$

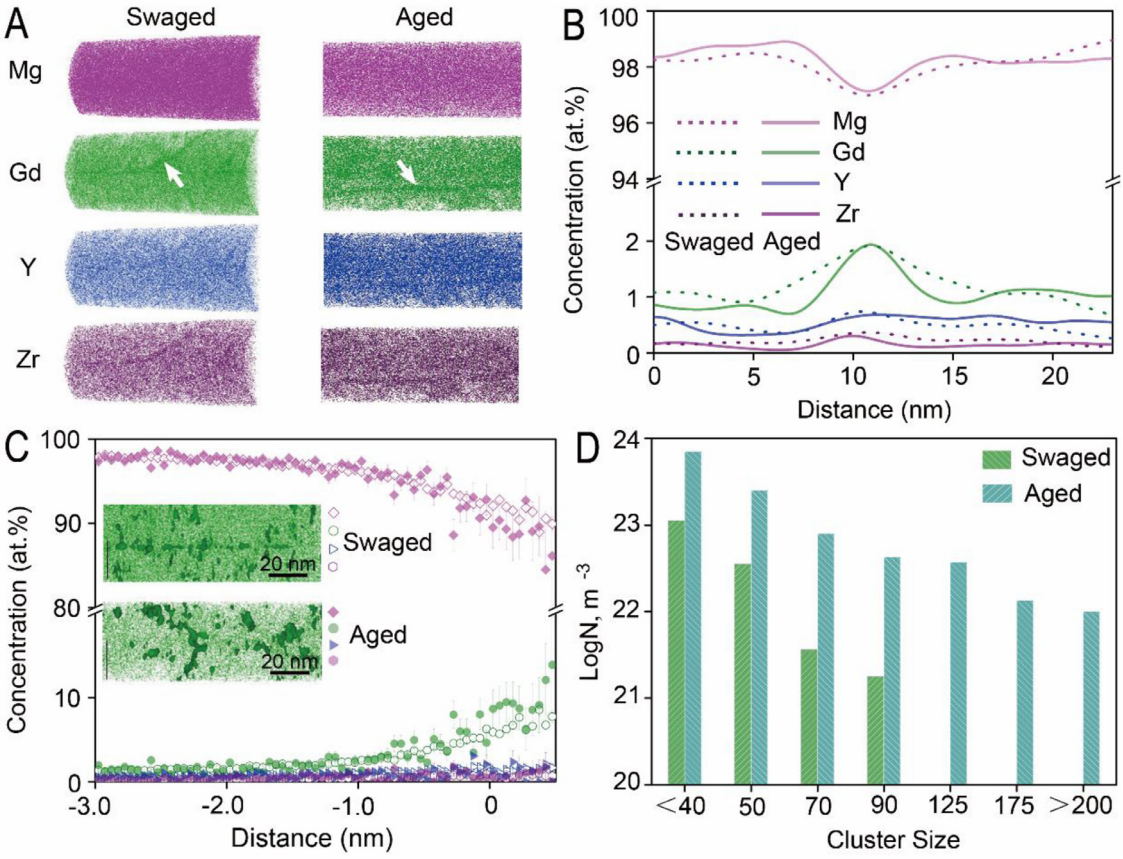

Fig. 9. Composition distributions of the solutes Gd, Y and Zr in the swaged and aged NC Mg alloys by APT. (A) Atomic maps of reconstructed volumes. (B) 1D concentration profiles across the GBs. (C) Proxigrams across the matrix/cluster interface. The insets are small-volume 3D atomic distributions of Gd with iso-surfaces (in green) at 4 at%. (D) Number density of the solute clusters *N* versus cluster size. (For interpretation of the references to color in this figure legend, the reader is referred to the web version of this article.)

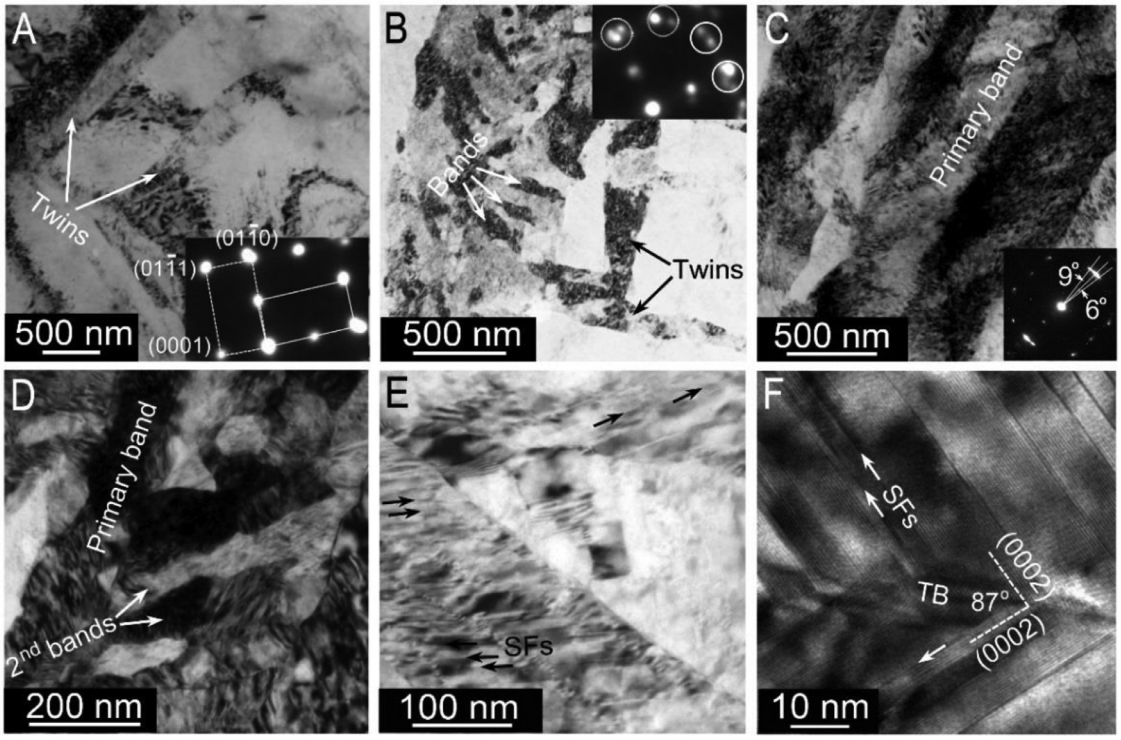

Fig. 10. Illustration of grain refinement mechanisms revealed by TEM in region I with different area reductions. (A) 6%, exhibiting the generation of {10$\bar{1}$2} tension twining. (B) 16%, the deformation twin plates were refined into finer sub-grain bands. The SAED pattern inset shows low-angle GBs between the sub-grain bands. (C) 6%, the non-twinned regions were refined into primary deformation bands. The SAED pattern inset shows low-angle GBs between the primary bands. (D) 16%, the primary bands were divided by dislocation arrays into secondary bands. (E and F) 26%, presenting a set of stacking faults (SFs) on (0001) plane.

Table 4
List of strengthening contributions from nano-grains σ_d, dislocations σ_ρ, solid solution σ_s and precipitation σ_{Orowan} of the aged NC Mg alloys.

Strengthening mechanisms	σ_d (MPa)	σ_ρ (MPa)	σ_s (MPa)	σ_{Orowan} (MPa)
Strengthening contributions	344	53	95	143

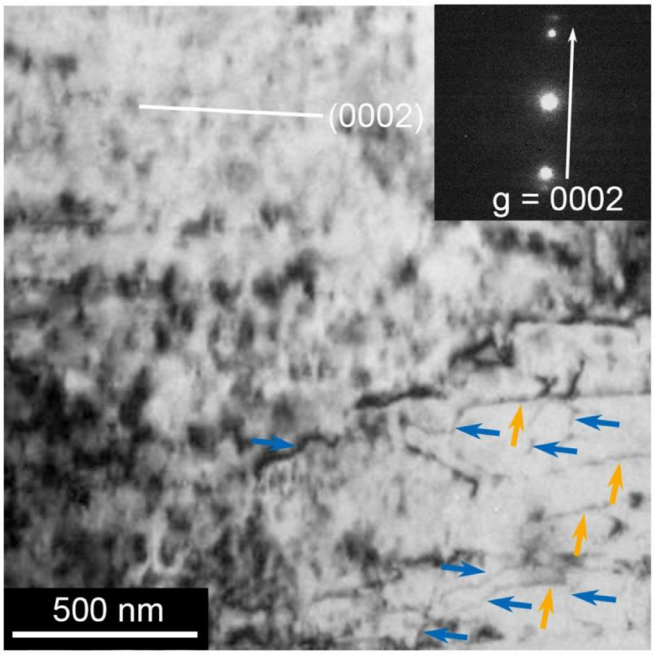

Fig. 11. Bright-field TEM image of the one-pass swaged alloy (area reduction of 6%) under two-beam diffraction. Basal <a> dislocations are invisible under diffraction vector $g = 0002$ based on $g \cdot b = 0$ criterion (b, Burgers vector). Dislocation segments lying on non-basal planes were indicated by orange and blue arrows, respectively. (For interpretation of the references to color in this figure legend, the reader is referred to the web version of this article.)

where ρ is the density of dislocations, equal to 0.3885×10^{15} m^{-2}, as calculated from the XRD pattern, b is the magnitude of the Burger's vector, equal to 0.3202 nm, α is a constant with a value of 0.24 [47], M is the Taylor Factor with a value of 2.1 [48]. Thus, $\sigma_\rho = 53$ MPa.

4.2.4. Precipitation strengthening contribution

The precipitation strengthening cintribution σ_{Orowan} was estimated based on the modified Orowan equation [49]

$$\sigma_{\text{Orowan}} = \frac{Gb}{2\pi\sqrt{1-\nu}\left(0.825\sqrt{\frac{d_t t_t}{f}} - 0.393 d_t - 0.886 t_t\right)} \times \ln\frac{0.886\sqrt{d_t t_t}}{b} \quad (5)$$

Here ν is the Poisson's ratio ($\nu = 0.35$). f is the volume fraction of the precipitates. d_t and t_t can be defined by the mean planar diameter d_p ($= \pi d_t/4$) and the mean planar thickness t_p ($= t_t$). d_p and t_p and f were determined to be 3.58 nm, 1.8 nm and 0.0161 from ATP results with Gd iso-surface at 7.5 at%. Thus, $\sigma_{Orowan} = 143$ MPa.

Briefly, based on the Hall-Petch equation, the strength of NC Mg was calculated at approximately 344 MPa for the 80 nm average grain size, and the strengthening contributions from dislocations, solid solution and precipitation were estimated as 53 MPa, 95 MPa and 143 MPa, respectively (Table 4). Compared with the experimental yield strength (650 MPa), the above calculation still exists a gap of 15 MPa which can be attributed to the strengthening from (iv) [32]. Five main deformation mechanisms are known to be expected in NC materials including preexisting dislocation gliding, GB dislocation emission, GB sliding and migration as well as grain rotation [26–29]. Firstly, the preexisting dislocations may be stabilized by forming Cottrell atmosphere-like solute clusters at the dislocation cores. Secondly, the GB segregation will strengthen the GB bond cohesion, which further slows dislocation nucleation at the GBs, GB sliding and migration as well as grain rotation. Moreover, the intra-granular solute clusters and β' precipitates could also provide effective resistance to slip of dislocations.

4.3. Intra-granular solute-clustering and inter-granular solute-segregation reactions

In literature, it has been reported that the Gd-rich clusters is detected in the as-quenched condition of solid solution treatment [50] suggesting Gd-rich clusters can be formed at room temperature in Mg alloys. Moreover, Zn- and Mg-rich solute clusters were also reported to form in Al alloys during long-term natural aging [51]. Nevertheless, we think the Gd-rich clusters dectected in the swaged Mg alloys were mainly formed during nanostructuring of swaging process and subsequent natural aging process (considering there is several months between swaging and APT). The reasons are as follows. First, the initially formed Gd-rich clusters are difficult to exist during SPD of swaging process and the solutes are susceptible to redistribution via solute-defects (dislocation, point defects and so on) interactions in order to lower the free energy of materials. During swaging process, the high concentration of mobile defects can sweep the Gd and Y solutes to GBs, and during subsequent natural aging, the Gd and Y solutes can further segregate at GBs and grain interiors through the enhanced diffusion process due to the presence of high-densities of lattice imperfections. Therefore, during swaging processing the lattice defects greatly influences the solute dispersion, and the resulting clusters and GB segregations reflect an energy landscape in which intra-granular solute-clustering and inter-granular solute-segregation reactions provide local reductions in free energy. Second, newly formed GB segregation of Gd and Y solutes after swaging process verified the solute diffusion ability to form intra-granular Gd rich clusters. Third, similar intra-granular solute-clustering and inter-granular solute-structuring reactions were observed in NC 7075 Al alloys after high pressure torsion processing at room temperature [30].

5. Conclusion

In this work, initial CG Mg-Gd-Y-Zr alloy rods were deformed by means of a conventional industrial method of rotary swaging process. The rotary swaged samples can be easily scaled up as the processing is continuous in length. Our work will advance the industrial applications of bulk NC Mg alloys by giving them a low-cost, energy-efficient and universal fabrication technique. Detailed results are summarized as follows:

1. Four-pass swaging produced a gradient microstructure and microharness in radial direction of which lattice defects increased from outer part to center part of the swaged rod. As a result, a NC region, with a dimension of ∅3 mm × 1000 mm, equi-axed grains of 80 nm in top plane

and NC lamella grains in side plane, was formed in the swaged rod center.

2. Tensile test indicated that the swaged NC Mg alloys had a remarkable high yield strength of 560 MPa, with the ultimate strength and ductility of 630 MPa and 5%, respectively. Fracture surface observation suggested a ductile intergranular fracture in the NC Mg alloys.
3. Low-temperature aging of the NC Mg alloys at a temperature of 448 K for 72 h did not change the grain size but precipitated β' phase in the nano-grain interior. As a result, the yield strength and ultimate tensile strength were further enhanced to 650 MPa and 710 MPa, respectively, the highest such values published for bulk Mg alloys.
4. APT analysis indicated that deformation of swaging led to Gd, Y and Zr solutes excess segregations at GBs and Gd-rich clusters in the nano-grain interior, whereas the low-temperature aging accelerated intra-granular cluster formation, resulting in a further increase in strength. The high concentration of mobile defects induced by swaging swept the solutes to GBs, and during subsequent natural and low-temperature aging, the solutes could further segregate at GBs and grain interiors due to the enhanced diffusion process.
5. The grain refinement of Mg alloy during swaging process included two stages: (i) CG subdivision into UFGs by twinning or dislocation slipping, (ii) further refinement of UFGs down to nano-grains by stacking faults and slipping.
6. Calculations indicated that the strengthening contributions from dislocations, solid solution, precipitation and nano-grain were estimated as 53 MPa, 95 MPa, 143 MPa and 344 MPa, respectively, among which the grain refinement strengthening mechanism played a dominant role.

Declaration of Competing Interest

The authors declare that they have no known competing financial interests or personal relationships that could have appeared to influence the work reported in this paper.

Acknowledgments

Y.H. Zhao acknowledges financial supports from National Key R&D Program of China (Grant No. 2017YFA0204403) and the National Natural Science Foundation of China (Grant Nos. 51971112 and 51225102) as well as the Fundamental Research Funds for the Central Universities (Grant No. 30919011405), Y.C. Wan, C.M. Liu, and G. Sha acknowledge financial supports from National Natural Science Foundation of China (Grants 51574291, 51874367, 51571120), China Postdoctoral Science Foundation (Grant number 2018M642999).

References

[1] P. Knochel, A flash of magnesium, Nat. Chem. 1 (2009) 740.
[2] T.M. Pollock, Weight loss with magnesium alloys, Science 328 (2010) 986–987.
[3] L.Y. Chen, J.Q. Xu, H. Choi, M. Pozuelo, X. Ma, S. Bhowmick, J.M. Yang, S. Mathaudhu, X.C. Li, Processing and properties of magnesium containing a dense uniform dispersion of nanoparticles, Nature 528 (2015) 539–543.
[4] G. Wu, J. Lu, K.C. Chan, L. Sun, L. Zhu, Dual-phase nanostructuring as a route to high-strength magnesium alloys, Nature 545 (2017) 80–83.
[5] A. Inoue, Y. Kawamura, M. Matsushita, K. Hayashi, J. Koike, Novel hexagonal structure and ultrahigh strength of magnesium solid solution in the Mg-Zn-Y system, J. Mater. Res. 16 (2001) 1894–1900.
[6] H.S. Jiang, X.G. Qiao, C. Xu, M.Y. Zheng, K. Wu, S. Kamado, Ultrahigh strength as-extruded Mg-10.3Zn-6.4Y-0.4Zr-0.5Ca alloy containing W phase, Mater. Des. 108 (2016) 391–399.
[7] T. Homma, N. Kunito, S. Kamado, Fabrication of extraordinary high-strength magnesium alloy by hot extrusion, Scr. Mater. 61 (2009) 644–647.
[8] D. Fang, G. Bi, L. Wang, G. Li, Z. Jiang, Microstructures and mechanical properties of Mg-2Y-1Mn-2Nd alloys fabricated by extrusion, Mater. Sci. Eng. A 527 (2010) 4383–4388.
[9] W. Jian, G. Cheng, W. Xu, H. Yuan, M. Tsai, Q. Wang, C.C. Koch, Y. Zhu, S. Mathaudhu, Ultrastrong Mg alloy via nano-spaced stacking faults, Mater. Res. Lett. 1 (2013) 61–66.
[10] Z. Yu, Y. Huang, X. Qiu, G. Wang, F. Meng, N. Hort, J. Meng, Fabrication of a high strength Mg-11Gd-4.5Y-1Nd-1.5Zn-0.5Zr (wt%) alloy by thermomechanical treatments, Mater. Sci. Eng. A 622 (2015) 121–130.
[11] R.G. Li, J.F. Nie, G.J. Huang, Y.C. Xin, Q. Liu, Development of high-strength magnesium alloys via combined processes of extrusion, rolling and ageing, Scr. Mater. 64 (2011) 950–953.
[12] S.V. Dobatkin, L.L. Rokhlin, E.A. Lukyanova, M.Y. Murashkin, T.V. Dobatkina, N.Y. Tabachkova, Structure and mechanical properties of the Mg-Y-Gd-Zr alloy after high pressure torsion, Mater. Sci. Eng. A 667 (2016) 217–223.
[13] H. Miura, G. Yu, X. Yang, Multi-directional forging of AZ61Mg alloy under decreasing temperature conditions and improvement of its mechanical properties, Mater. Sci. Eng. A 528 (2011) 6981–6992.
[14] W.J. Kim, I.B. Park, S.H. Han, Formation of a nanocomposite-like microstructure in Mg-6Al-1Zn alloy, Scr. Mater. 66 (2012) 590–593.
[15] W.J. Kim, H.G. Jeong, H.T. Jeong, Achieving high strength and high ductility in magnesium alloys using severe plastic deformation combined with low-temperature aging, Scr. Mater. 61 (2009) 1040–1043.
[16] W. Kim, S. Hong, Y. Kim, S. Min, H. Jeong, J. Lee, Texture development and its effect on mechanical properties of an AZ61 Mg alloy fabricated by equal channel angular pressing, Acta Mater. 51 (2003) 3293–3307.
[17] Z. Wu, W.A. Curtin, The origins of high hardening and low ductility in magnesium, Nature 526 (2015) 62–67.
[18] W. Xu, N. Birbilis, G. Sha, Y. Wang, J.E. Daniels, Y. Xiao, M. Ferry, A high-specific-strength and corrosion-resistant magnesium alloy, Nat. Mater. 14 (2015) 1229–1235.
[19] Z. Wu, R. Ahmad, B. Yin, S. Sandlobes, W.A. Curtin, Mechanistic origin and prediction of enhanced ductility in magnesium alloys, Science 359 (2018) 447–452.
[20] B.Y. Liu, F. Liu, N. Yang, X.B. Zhai, L. Zhang, Y. Yang, B. Li, J. Li, E. Ma, J.F. Nie, Z.W. Shan, Large plasticity in magnesium mediated by pyramidal dislocations, Science 365 (2019) 73–75.
[21] J. Li, Z. He, P. Fu, Y. Wu, L. Peng, W. Ding, Heat treatment and mechanical properties of a high-strength cast Mg-Gd-Zn alloy, Mater. Sci. Eng. A 651 (2016) 745–752.
[22] Y. Zhang, Y. Wu, L. Peng, P. Fu, F. Huang, W. Ding, Microstructure evolution and mechanical properties of an ultra-high strength casting Mg-15.6Gd-1.8Ag-0.4Zr alloy, J. Alloys Compd. 615 (2014) 703–711.
[23] H.Q. Sun, Y.N. Shi, M.X. Zhang, K. Lu, Surface alloying of an Mg alloy subjected to surface mechanical attrition treatment, Surf. Coat. Technol. 202 (2008) 3947–3953.
[24] Z. Yang, et al., Precipitation process and effect on mechanical properties of Mg–9Gd–3Y–0.6Zn–0.5Zr alloy, Mater. Sci. Eng. A 454–455 (2007) 274–280.
[25] Z. Yang, J.P. Li, Y.C. Guo, T. Liu, F. Xia, Z.W. Zeng, M.X. Liang, Precipitation process and effect on mechanical properties of Mg-9Gd-3Y-0.6Zn-0.5Zr alloy, Mater. Sci. Eng. A 454-455 (2007) 274–280.
[26] J. Schiøtz, F.D.D. Tolla, K.W. Jacobsen, Softening of nanocrystalline metals at very small grain sizes, Nature 391 (1998) 561–563.
[27] T.J. Rupert, D.S. Gianola, Y. Gan, K.J. Hemker, Experimental observations of stress-driven grain boundary migration, Science 326 (2009) 1686–1690.
[28] Z. Shan, E.A. Stach, J.M. Wiezorek, J.A. Knapp, D.M. Follstaedt, S.X. Mao, Grain boundary-mediated plasticity in nanocrystalline nickel, Science 305 (2004) 654–656.
[29] M.-S. Colla, B. Amin-Ahmadi, H. Idrissi, L. Malet, S. Godet, J.-P. Raskin, D. Schryvers, T. Pardoen, Dislocation-mediated relaxation in nanograined columnar palladium films revealed by on-chip time-resolved HRTEM testing, Nat. Commun. 5 (2015) 5922.
[30] P.V. Liddicoat, X.Z. Liao, Y. Zhao, Y. Zhu, M.Y. Murashkin, E.J. Lavernia, R.Z. Valiev, S.P. Ringer, Nanostructural hierarchy increases the strength of aluminium alloys, Nat. Commun. 1 (2010) 63.
[31] J. Nie, Y. Zhu, J. Liu, X.-Y. Fang, Periodic segregation of solute atoms in fully coherent twin boundaries, Science 340 (2013) 957–960.
[32] J. Hu, Y.N. Shi, X. Sauvage, G. Sha, K. Lu, Grain boundary stability governs hardening and softening in extremely-fine nanograined metals, Science 355 (2017) 1292–1296.
[33] H. Sun, Y.-N. Shi, M.-X. Zhang, K. Lu, Plastic strain-induced grain refinement in the nanometer scale in a Mg alloy, Acta Mater. 55 (2007) 975–982.
[34] Y.B. Wang, X.Z. Liao, Y.H. Zhao, E.J. Lavernia, S.P. Ringer, Z. Horita, T.G. Langdon, Y.T. Zhu, The role of stacking faults and twin boundaries in grain refinement of a Cu-Zn alloy processed by high-pressure torsion, Mater. Sci. Eng. A 527 (2010) 4959–4966.
[35] K. Oh-ishi, C.L. Mendis, T. Homma, S. Kamado, T. Ohkubo, K. Hono, Bimodally grained microstructure development during hot extrusion of Mg-2.4Zn-0.1Ag-0.1Ca-0.16 Zr (at.%) alloys, Acta Mater. 57 (2009) 5593–5604.
[36] L.L. Tang, Y.H. Zhao, J. Rinat, Y. Cao, R.Z. Valiev, E.J. Lavernia, Y.T. Zhu, Enhanced strength and ductility of AZ80 Mg alloys by spray forming and ECAP techniques, Mater. Sci. Eng. A 670 (2016) 280–291.
[37] X. Luo, Z.Q. Feng, T.B. Yu, J.Q. Luo, T.L. Huang, G.L. Wu, N. Hansen, X.X. Huang, Transitions in mechanical behavior and in deformation mechanisms enhance the strength and ductility of Mg-3Gd, Acta Mater. 183 (2020) 398–407.
[38] H.C. Xiao, S.N. Jiang, B. Tang, W.H. Hao, Y.H. Gao, Z.Y. Chen, C.M. Liu, Hot deformation and dynamic recrystallization behaviors of Mg-Gd-Y-Zr alloy, Mater. Sci. Eng. A 628 (2015) 311–318.

[39] L. Tang, W. Liu, Z. Ding, D. Zhang, Y. Zhao, E.J. Lavernia, Y. Zhu, Alloying Mg with Gd and Y: Increasing both plasticity and strength, Comp. Mater. Sci. 115 (2016) 85–91.
[40] S.Q. Zhu, H.G. Yan, X.Z. Liao, S.J. Moody, G. Sha, Y.Z. Wu, S.P. Ringer, Mechanisms for enhanced plasticity in magnesium alloys, Acta Mater. 82 (2015) 344–355.
[41] E.W. Hart, Theory of the tensile test, Acta Met. 15 (1967) 351–355.
[42] Q. Wei, S. Cheng, K.T. Ramesh, E. Ma, Effect of nanocrystalline and ultrafine grain sizes on the strain rate sensitivity and activation volume: fcc versus bcc metals, Mater. Sci. Eng. A 381 (2004) 71–82.
[43] M. Mabuchi, K. Higashi, Strengthening mechanisms of Mg Si alloys, Acta Mater. 44 (1996) 4611–4618.
[44] L.L. Rokhlin, Magnesium Alloys Containing Rare Earth Metals: Structure and Properties, CRC Press, 2003.
[45] Y.H. Zhao, K. Zhang, K. Lu, Structure characteristics of nanocrystalline element selenium with different grain sizes, Phys. Rev. B 56 (1997) 14322–14329.
[46] X.C. Liu, H.W. Zhang, K. Lu, Strain-induced ultrahard and ultrastable nanolaminated structure in nickel, Science 342 (2013) 337–340.
[47] N. Hansen, X. Huang, Microstructure and flow stress of polycrystals and single crystals, Acta Metall. 46 (1998) 1827–1836.
[48] C.H. Cáceres, P. Lukáč, Strain hardening behaviour and the Taylor factor of pure magnesium, Philps. Mag. 88 (2008) 977–989.
[49] J. Nie, Effects of precipitate shape and orientation on dispersion strengthening in magnesium alloys, Scr. Mater 48 (2003) 1009–1015.
[50] J.F. Nie, K. Oh-ishi, X. Gao, K. Hono, Solute segregation and precipitation in a creep-resistant Mg-Gd-Zn alloy, Acta Mater. 56 (2008) 6061–6076.
[51] J.Z. Liu, R. Hu, J. Zheng, Y. Zhang, Z. Ding, W. Liu, Y.T. Zhu, G. Sha, J. Alloys Compd. 821 (2020) 153572.